Monthly Notices
of the
ROYAL ASTRONOMICAL SOCIETY

MNRAS **494,** 4057–4068 (2020)
Advance Access publication 2020 April 21

doi:10.1093/mnras/staa1055

Evidence for variability time-scale-dependent UV/X-ray delay in Seyfert 1 AGN NGC 7469

Mayukh Pahari [1]★ I. M. McHardy,[1] Federico Vincentelli [1] Edward Cackett,[2] Bradley M. Peterson,[3,4] Mike Goad,[5] Kayhan Gültekin[6] and Keith Horne[7]

[1]*School of Physics & Astronomy, University of Southampton, Highfield Campus, Southampton SO17 1BJ, UK*
[2]*Department of Physics and Astronomy, Wayne State University, 666 W. Hancock Street, Detroit, MI 48201, USA*
[3]*Department of Astronomy, The Ohio State University, 140 W 18th Avenue, Columbus, OH 43210, USA*
[4]*Space Telescope Science Institute, 3700 San Martin Drive, Baltimore, MD 21218, USA*
[5]*Department of Physics and Astronomy, University of Leicester, Leicester LE1 7RH, UK*
[6]*Department of Astronomy, University of Michigan, 500 Church Street, Ann Arbor, MI 48109, USA*
[7]*School of Physics and Astronomy, University of St. Andrews, Fife KY16 9SS, UK*

Accepted 2020 April 16. Received 2020 April 10; in original form 2019 September 16

ABSTRACT

Using a month-long X-ray light curve from *RXTE*/PCA and 1.5 month-long UV continuum light curves from *IUE* spectra in 1220–1970 Å, we performed a detailed time-lag study of the Seyfert 1 galaxy NGC 7469. Our cross-correlation analysis confirms previous results showing that the X-rays are delayed relative to the UV continuum at 1315 Å by 3.49 ± 0.22 d, which is possibly caused by either propagating fluctuation or variable Comptonization. However, if variations slower than 5 d are removed from the X-ray light curve, the UV variations then lag behind the X-ray variations by 0.37 ± 0.14 d, consistent with reprocessing of the X-rays by a surrounding accretion disc. A very similar reverberation delay is observed between *Swift*/XRT X-ray and *Swift*/UVOT *UVW2*, *U* light curves. Continuum light curves extracted from the *Swift*/GRISM spectra show delays with respect to X-rays consistent with reverberation. Separating the UV continuum variations faster and slower than 5 d, the slow variations at 1825 Å lag those at 1315 Å by 0.29 ± 0.06 d, while the fast variations are coincident (0.04 ± 0.12 d). The UV/optical continuum reverberation lag from *IUE*, *Swift*, and other optical telescopes at different wavelengths are consistent with the relationship: $\tau \propto \lambda^{4/3}$, predicted for the standard accretion disc theory while the best-fitting X-ray delay from *RXTE* and *Swift*/XRT shows a negative X-ray offset of ∼0.38 d from the standard disc delay prediction.

Key words: accretion, accretion discs – black hole physics – galaxies: individual: NGC 7469 – galaxies: Seyfert – X-rays: galaxies.

1 INTRODUCTION

Emission-line reverberation mapping (Blandford & McKee 1982; Peterson 2014), based on measured lags between continuum and emission-line bands and the width of the emission line, is a very successful technique for determining active galactic nucleus (AGN) broad-line region (BLR) size and black hole virial mass. Over 60 masses have currently been measured (Peterson et al. 2004; Bentz et al. 2009; Bentz & Katz 2015). Over the last 2 decades, considerable observational effort has also been put into continuum reverberation mapping, measuring the lags between a short-wavelength band, often the X-rays, and longer wavelength UV and optical bands. The initial aim was to map the temperature structure of the accretion disc and hence find a standard candle by which distances could be estimated and the Hubble constant derived (Cackett, Horne & Winkler 2007). Most such studies assumed a disc with the temperature structure as derived by Shakura & Sunyaev (1973). Incident high-energy emission will enhance the existing thermal emission leading to a wavelength (λ) dependent lag, τ, between the incident high energy, and re-radiated UV/optical emission, of $\tau \propto (M^2 \dot{m}_E)^{1/3} \lambda^{\beta}$ where $\beta = 4/3$, M is the black hole mass, and $\dot{m}_E$ is the accretion rate in Eddington units. Initial studies (Collier et al. 1999; Cackett et al. 2007) were consistent with $\beta = 4/3$, but included only optical bands and did not extend to the X-ray bands.

Coordinated observations, usually with Rossi X-ray Timing Explorer (*RXTE*; McHardy et al. 2003; Shemmer et al. 2003; Uttley et al. 2003; Arev´alo et al. 2008; Marshall, Ryle & Miller 2008;

★ E-mail: M.Pahari@soton.ac.uk

Arev´alo et al. 2009; Breedt et al. 2009), and ground-based optical telescopes, mostly revealed a good correlation, with the optical lagging behind the X-rays, consistent with the expectations of reprocessing. However, the lag measurements $\sim 1 \pm 0.5$ d were rarely statistically significant and could not rule out that the X-rays might lag behind the optical. These long *RXTE*-based programmes, which in some cases covered up to 10 yr (Breedt et al. 2010), also showed that although there was a good correlation between the X-rays and the optical bands on short time-scales (weeks–months), on longer time-scales (months–years) there were often trends in the optical light curves with no counterparts in the X-ray light curves.

Lags in the opposite sense, where the hard band lags the soft, are also seen on longer time-scales. These hard lags have been seen in both X-ray binaries (from milliseconds to seconds) and AGNs (from days to months) (Papadakis, Nandra & Kazanas 2001; McHardy et al. 2004; Arev´alo & Uttley 2006), and are thought to arise due to the inward propagation on viscous time-scales of mass accretion fluctuations in the disc that are then transmitted to the corona (Kotov, Churazov & Gilfanov 2001; Arev´alo & Uttley 2006; Uttley et al. 2011).

More intense, multiband, observations with *Swift* (McHardy et al. 2014; Shappee et al. 2014; Edelson et al. 2015; Fausnaugh et al. 2016; Troyer et al. 2016; Edelson et al. 2017; McHardy et al. 2018; Pal & Naik 2018; Edelson et al. 2019) confirmed the general picture of wavelength-dependent UV/optical lags, consistent with disc reprocessing, although the measured lags were ∼2–3 times longer than expected theoretically (McHardy et al. 2014). This discrepancy may indicate an inhomogeneous disc (Dexter & Agol 2011). The *Swift* observations also provide evidence of reprocessing of high-energy emission from a larger reprocessor than just the accretion disc, probably the BLR clouds (Cackett et al. 2018; Lawther et al. 2018; McHardy et al. 2018; Pal & Naik 2018; Sun et al. 2018; Chelouche, Pozo & Francisco 2019; Korista & Goad 2019). This evidence is in the form of an excess lag in the *U* band (Edelson et al. 2015; Fausnaugh et al. 2016; Edelson et al. 2017), which contains the Balmer continuum, (Korista & Goad 2001) and an excess lag at 3634 Å (known as the Balmer jump), and also in the fact that the reprocessing function required to explain the optical emission as reprocessing of X-ray emission, has a tail to long delays (a few days) as well as a sharp peak at short time-scales (∼hours) from the disc. The *Swift* observations also show that although wavelength-dependent lags following roughly $\tau \propto \lambda^{4/3}$ apply in most AGNs between the UV and optical bands, the lag between the X-ray and UV band is usually much larger than expected purely from extrapolation of the UV-optical lag spectrum down to X-ray wavelengths (Dai et al. 2010; Morgan et al. 2010; Mosquera et al. 2013; Edelson et al. 2015; Fausnaugh et al. 2016; McHardy et al. 2018). Moreover, the X-ray/UV correlation is weaker than the UV/optical one (Edelson et al. 2019).

There are a number of possible explanations for this increased lag, including that the lag corresponds to the thermal time-scale due to the thermal reverberation from a significantly hot disc with low accretion rate (Sun et al. 2018; Kammoun et al. 2019), hot accretion flow with a disc truncation (Noda et al. 2016), very large area of the reprocessing site (Pal et al. 2017; Pal & Naik 2018), non-blackbody nature of the emerging disc spectra due to the low atmospheric density (Hall, Sarrouh & Horne 2018). Other potential explanations include that the X-rays do not directly illuminate the outer disc but are first reprocessed by, and scattered through, the scattering atmosphere (Narayan 1996), the inflated inner edge of the accretion disc, which introduces an additional lag (Gardener & Done 2017).

The increase in X-ray/UV-optical correlation strength on short time-scales, originally noted by Breedt et al. (2009), has also been noted in *Swift* observations. For example, in NGC 5548 when variations on time-scales longer than 20 d are removed from UV light curves, the correlation improves and, moreover, the X-ray to UV lag now falls on an extrapolation of the UV-optical lag spectrum. A similar behaviour is seen in NGC 4593 (McHardy et al. 2018) where the X-ray/UV lag decreases when long time-scale variations (>10 d), presumably from the BLR, are removed from the UV light curves. The resultant X-ray/UV lag is then again in agreement with an extrapolation of the UV-optical lag spectrum to X-ray wavelengths.

The one notable exception to the general scenario that the UV/optical variations on short time-scales are mainly driven by reprocessing of high-energy (i.e. X-ray) variations is NGC 7469, a bright, infrared luminous, Sb-type spiral Seyfert 1 galaxy at a redshift of 0.016268. The mass of the central supermassive black hole is $9.04^{+1.06}_{-0.97} \times 10^6$ $M_\odot$[1] (Zu, Kochanek & Peterson Bradley 2011; Peterson et al. 2014).

In 1996 June–July, NGC 7469 was observed almost continuously, Earth occultations excepted, for a period of ∼46 d by *IUE*, providing UV spectra from which light curves can be produced in a variety of bands (Wanders et al. 1997). For 30 of these days there was almost continuous *RXTE*/PCA monitoring. Both the *IUE* and *RXTE* light curves are dominated by a small number of large amplitude, quasi-sinusoidal, variations with peak to peak time-scales of around 15–20 d (see fig. 2 of Nandra et al. 1998). Nandra et al. (1998) show that the peaks in the UV light curve led the peak in the X-rays by ∼4 d. Although there are only two cycles of variability in this analysis, these observations none the less led to much speculation regarding physical mechanisms which might explain the 4 d X-ray lag. Nandra et al. (1998) suggested that the X-rays might be produced by upscattering of UV photons by a variable coronal structure. Using the same UV/X-ray observations, Petrucci et al. (2004) performed UV and hard X-ray joint spectral fitting and found an anticorrelation between the UV flux and the X-ray coronal temperature. The explanation of such an anticorrelation requires strong variability in coronal structure over days rather than a simple disc–corona structure (Petrucci et al. 2004).

However, just within the *IUE* band, Wanders et al. (1997) estimated the delay of Ly α, C IV, N V, Si IV, and He II emission lines with respect to the UV continuum as 2.3–3.1, ∼2.7, 1.9–2.4, 1.7–1.8, and 0.7–1 d, respectively, which are broadly consistent with observations of other Seyfert galaxies. Using concurrent ground-based spectrophotometric monitoring of NGC 7469, Collier et al. (1998) found that continuum variations at 4865 and 6962 Å lag those at 1315 Å by 1.0 ± 0.3 and 1.5 ± 0.7 d, respectively. They also noted that the continuum variations at 1485–1825 Å lag those at 1315 Å by 0.21–0.35 d, which are consistent with the expectations from disc reprocessing. Later, using a more sophisticated spectral modelling approach, using the *HST*/FOS spectrum as a template, Kriss et al. (2003) found that the continuum variations at 1485, 1740, and 1825 Å are delayed relative to the shorter UV continuum at 1315 Å by 0.09, 0.29, and 0.36 d, respectively, again in good agreement with disc reprocessing.

The main remaining unexplained problem therefore is the relationship between the X-ray and UV variations. In this paper, we

[1]This neglects a further ∼0.4 dex uncertainty due to using the population mean value of the dimensionless factor *f*, which depends on the uncertain geometry and orientation of the BLR in each object.

Table 1. Details of observations from different telescopes and satellites used in this work. Central wavelengths and FWHM (Poole et al. 2008) are quoted in case of *UVW2* and *U* filters.

Telescope/ Instrument	Observation time (MJD)	No. of exposures /data points	Wavelength coverage (Å)
RXTE/PCA	50244–50275	311	0.83–6.22
IUE	50244–50294	218	1150–1975
Swift/XRT	54630–58230	176	1.24–24.8
Swift/UVOT			
UVW2	54644–58229	98	1928 ± 657
U	54635–57423	61	3465 ± 785
UV-GRISM	56410–56524	37	1700–2900
Wise/FOSC[a]	50237–50295	42	4016–7841

[a]AGN Watch campaign.

re-examine the relationship between the X-ray and UV variations as observed by *RXTE* and *IUE*. In addition to examining the correlation in the raw light curves, we also search for a correlation in light curves from which the long time-scale, large amplitude, variations have been removed (Section 3). Here, we find lags that are more consistent with the reprocessing scenario (Section 4.1). We also examine archival *Swift* data which, although with considerably greater uncertainties than in the *IUE* data, allow us to extend our lag measurements into the optical bands (Section 5). These data also allow us to determine whether the apparent lag of the UV by the X-rays seen with *IUE* and *RXTE*, when considering long time-scale variations, is a common phenomenon. This does not appear to be the case. We compare the observed wavelength-dependent lag with that predicted. We conclude the paper (Section 7) with a brief summary of the observational results and with some general overall interpretations.

2 OBSERVATION

RXTE performed 311 observations of NGC 7469 between 1996 June 10 00:44:16 and July 11 23:59:19. For each observation, we extract the *RXTE*/PCA light curve in the 2–15 keV energy range, combining observations from PCU0, PCU1, and PCU2 which were operational during the entire period of the observations. *IUE* continuously monitored NGC 7469 between 1996 June 10 and July 29 producing in total of 218 low-dispersion UV spectra in the wavelength range of 1150–1975 Å. The details of the analysis procedure are provided in Wanders et al. (1997). Raw images were processed using the TOMSIPS (Ayres 1993) and NEWSIPS (Nichols et al. 1993) data reduction packages. In this work, we consider NEWSIPS pipeline reduced spectra as mentioned by Wanders et al. (1997), a non-linear wavelength calibration error exists in TOMSIPS reduction since long-term drifts in the wavelength scale were not taken into account. On the other hand, NEWSIPS reduced spectra matches well with the *HST* spectra without any corrections applied. We also use data from *Swift* and the Wise Observatory optical telescope that are described later. Details of observations that are used to perform continuum reverberation mapping are provided in Table 1.

3 DATA REDUCTION

Light-curve extractions are performed using HEASOFT `6.25` packages applying standard filtering criteria. Further details on the observation and analysis procedures are provided by Nandra et al. (1998).

In case of NEWSIPS pipeline reduced *IUE* spectra, due to a small shift (1–2 Å) in wavelength caused by the large aperture pointing errors (Wanders et al. 1997), an offset compensation is performed so that the sharp C IV line feature of all spectra falls at same average wavelength. Extinction corrections are not significant due to the very low interstellar reddening $E(B-V) = 0.059$ and background corrections are applied. The redshift observed from the C IV average peak is consistent with the spectroscopic redshift of $z = 0.00163$ from the [O III] line at 5007 Å (Salamanca, Alloin & Pelat 1995).

3.1 UV spectral fitting

IUE UV spectra show significant variability in the continuum flux level. An example of such variations is shown in the left-hand panel of Fig. 1. At all wavelengths between 1220 and 1970 Å, the continuum UV flux as observed on 1996 June 15 is significantly higher than that on 1996 June 19. To study flux variability, we extract light curves at different wavelengths. To extract UV continuum and line light curves from UV spectra, we adopt a slightly different approach than Wanders et al. (1997). Using the χ^2 minimization technique in XSPEC, we fit the average spectrum with suitable combinations of a power-law function that represents the underlying continuum and multiple narrow and broad Gaussian components that describe emission lines. The best-fitting model yields residuals with χ^2 per degrees of freedom = 179/175. The right-hand panel of Fig. 1 shows the time-averaged UV spectrum fitted with different model components and the residual of the fitting. The power-law energy spectral index from the best-fitting average UV spectrum is observed to be -1.67 ± 0.11 which is consistent with that typically observed from AGNs (Shull et al. 2012) and also consistent with the radio-quiet nature of NGC 7469 (Baldi et al. 2015). Using the best-fitting model, we fit individual *IUE* spectra by fixing the continuum power-law index and letting all other parameters vary. From individual spectrum fitting, we derive spectral line and continuum parameters such as line width and flux. One advantage of using spectral modelling over numerical integration is that line and continuum fluxes can be measured more accurately, particularly when narrow/broad lines are close to each other and there exists an underlying broad continuum. For example, Vestergaard & Wilkes (2001) showed that the asymmetry in the blue wing of the C IV line is caused by the presence of high-ionization Si II lines at ∼1540 Å. Therefore, the use of two Gaussian components at both line locations provide more accurate modelling and hence flux measurements of the underlying continuum. From the best-fitting model, continuum UV flux is computed in the rest-frame wavelength range of 1306–1327, 1473–1495, 1730–1750, and 1805–1835 Å using a convolution model (`cflux` in XSPEC) that provides integrated, continuum-subtracted flux over a given wavelength range and its 1σ error. Wavelength ranges for continuum flux measurement are kept consistent with those from Wanders et al. (1997).

3.2 Filtering

In this paper, we are searching for signs of reprocessing in the original *RXTE* and *IUE* observations, which are dominated by a very small number (two in the X-ray observations, three in the *IUE* campaign) of large amplitude variations with peak to trough time-scales of ∼10 d. If NGC 7469 behaves like other AGNs of similar mass and accretion rate, the reprocessing signature should be manifest by the UV lagging the X-ray light curves by less than a day. It is well established that long-term variations can distort

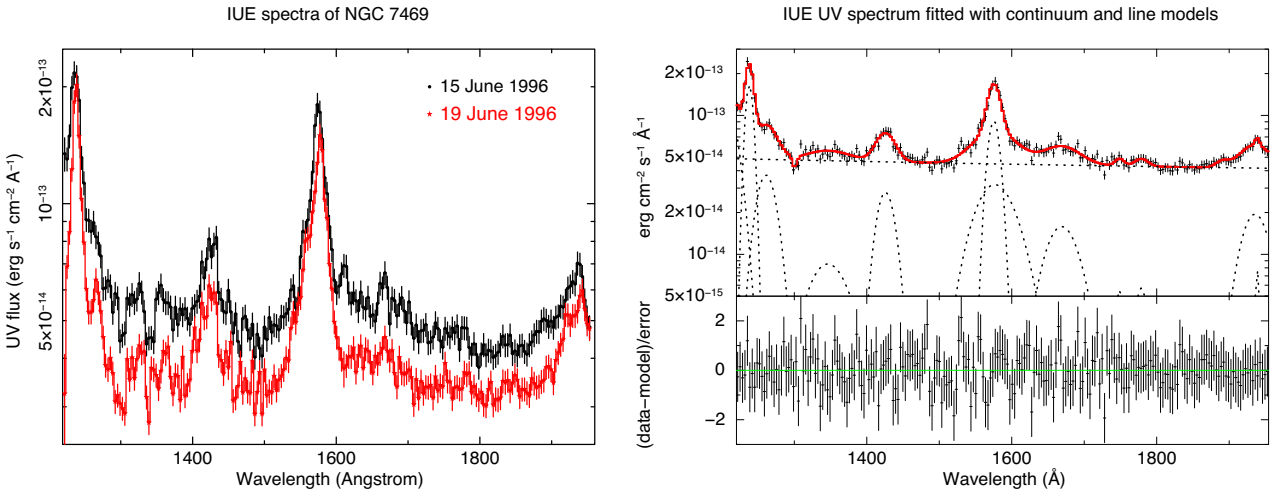

Figure 1. UV variability of NGC 7469 and spectral modelling: Left: *IUE* spectra of the NGC 7469 nucleus in the wavelength range of 1220–1970 Å as observed on 1996 June 15 (circles) and June 19 (stars), respectively. A substantial decrease is observed in the UV continuum flux level within 4 d. Right: the best-fitting time-averaged UV spectrum (1220–1970 Å) from *IUE* fitted with a model (red) consisting of a continuum, broad, and narrow emission features and narrow absorption (dotted lines; top) and the residual of the fitting (bottom). Each of 218 spectra is fitted separately with the best-fitting model to obtain the UV continuum and line fluxes from each pointing.

the measurement of short-term lags in cross-correlation function (CCFs; Welsh 1999) and so we filter out the long time-scale, large amplitude, and variations. We choose a 5-d filtering time-scale that will eliminate variations on longer time-scales but will allow lags on time-scales shorter than 5 d, of both positive (i.e. reprocessing) and negative (seed photon variation) sign, to be detected. Similar filtering techniques have been used successfully to reveal short time-scale correlations in other AGNs, e.g. NGC 5548 (McHardy et al. 2014) and NGC 4593 (McHardy et al. 2018).

To filter the light curves, we use a locally weighted scatter plot smoothing (LOWESS) function that is based upon a non-parametric, non-linear least-squares regression method (Cleveland & Devlin 1988). The weight function used for LOWESS is the tricube kernel function: $k(d) = (1 - |d|^3)^3$ where d is the distance of a given data point from the point on the curve being fitted, scaled to lie in the range from 0 to 1. For the filtering purpose, $d(t) \equiv (t - t_i)/\Delta t$ is the time difference between time t and the data point i at time t_i in units of $\Delta t = 5$ d. Such a function has higher efficiency than traditional kernel functions like boxcar or triangular and does not require specification of the model function to fit the data therefore making it ideal to fit complex processes where no theoretical model exists. When compared to the efficiency of the Epanechnikov kernel function, the relative efficiency of the LOWESS kernel is 99.8 per cent while the same for the boxcar and triangular kernels are 92.9 per cent and 98.6 per cent, respectively (Epanechnikov 1969). The efficiency of a function f(x) is defined as $\sqrt{\int x^2 f(x) dx}$ $\int f(x)^2 \mathrm{d}x$.

In this work, the LOWESS filter is used (residual from the LOWESS function fitting) to eliminate variability slower than 5 d in the X-ray and UV light curves. In the rest of the paper and in all Figures, the word 'filtered' implies a 5-d filtering unless otherwise specified.

3.3 Correlation and delay measurements

Since X-ray and UV observations have dissimilar temporal coverage, we use the interpolated CCF to compute the delay among X-ray and various UV continuum and line light curves. Uncertainties on lag measurements are computed using a Monte Carlo simulation to assess the flux uncertainties associated with each measurement and the sampling uncertainties of the observed time series, similar to bootstrapping. The details of the implementation of both methods are provided in Peterson et al. (1998) and denoted as the flux randomization (FR) and random subset selection (RSS) methods, respectively. For each Monte Carlo realization of a light curve with N data points, N selections are drawn at random (i.e. random subset selection or RSS); for data points that are randomly selected multiple times M, the associated uncertainty is decreased by $M^{1/2}$. The data points are then altered by adding random Gaussian deviates with a dispersion equal to the assigned flux uncertainty (i.e. FR). Multiple realizations result in a distribution of CCFs, and the corresponding joint distribution of CCF peak correlation coefficients and centroid lags. Centroid lag ($\tau_{\rm cent}$) is computed by averaging lag over regions where CCF is above 80 per cent of the peak.

We perform 100 000 FR + RSS simulations for each pair of X-ray/UV light curves in this work and consider only measurements for which the cross-correlation coefficient is higher than 0.2. Although the resultant lag distribution may deviate from the normal distribution, we fit the resulting CCF centroid distribution using a Gaussian function and interpret the Gaussian centre as the measured time delay and its half width at half-maxima (FWHM/2) as the uncertainty on the delay measurements.

4 ANALYSIS AND RESULTS

The left-hand panel of Fig. 2 shows the 2–15 keV X-ray light curve (top) and the 1306–1327 Å UV continuum light curve (bottom; referred here 1315 Å band) observed with *RXTE* and *IUE*, respectively. Both light curves are shown as residuals after subtracting the mean flux for comparison of light-curve variability relative to their mean value. The right-hand panel shows the centroid lag distribution of the FR + RSS cross-correlation between the X-ray and UV continuum light curves. The cross-correlation distribution peak indicates that X-rays are delayed relative to the UV 1315 Å band continuum by 3.49 ± 0.22 d. This is consistent

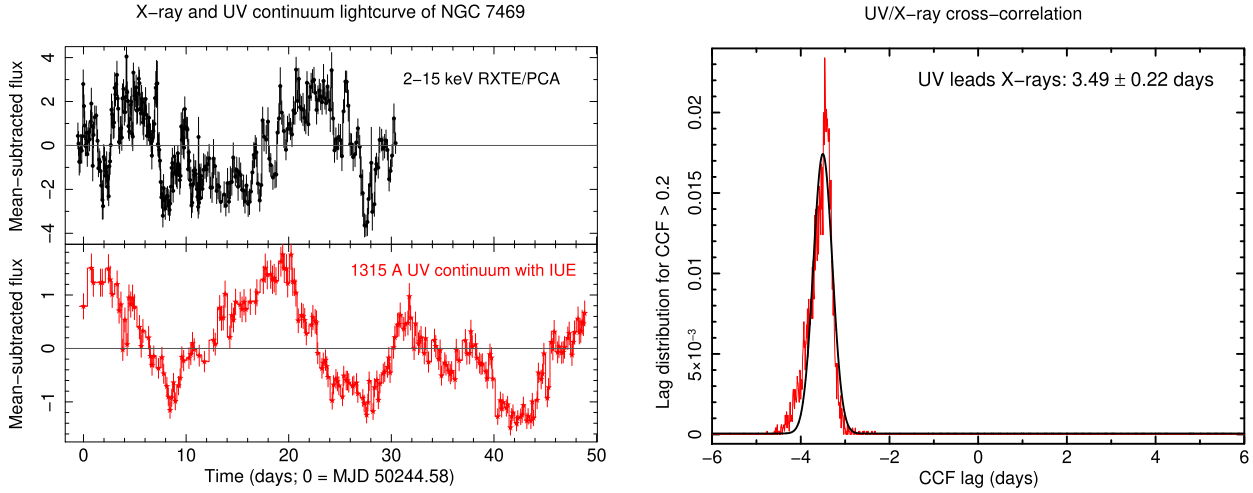

Figure 2. X-ray/UV cross-correlation: Left: 2–15 keV background-subtracted *RXTE*/PCA light curve (top) and rest-frame 1315 Å UV continuum light curve observed with *IUE* (bottom). Both light curves are mean subtracted for a better visibility of the relative flux variability. When both light curves are cross-correlated using Monte Carlo-based combined FR and RSS methods, the relative frequency distribution of the CCF centroids (when cross-correlation coefficient >0.2) is shown in the right-hand panel. The lag distribution is fitted with a Gaussian. The centroid and the FWHM/2 of the Gaussian with stronger peak are quoted as the time delay and its uncertainty, respectively.

with previous measurements by Nandra et al. (1998) but inconsistent with reprocessing models in which the UV variations should lag the X-rays.

4.1 Effect of light-curve filtering

The filtered X-ray and UV light curves are shown in the left-hand panel of Fig. 3. Visually the light curves are now quite similar. An FR + RSS cross-correlation between filtered light curves along with the CCF, shown in the right-hand panel of Fig. 3, clearly demonstrates that on a time-scale faster than 5 d, the UV continuum lags the X-rays by 0.37 ± 0.14 d. The solid black line in the right-hand panel of Fig. 3 shows the interpolated CCF (White & Peterson 1994) for the light curves in the left-hand panel of Fig. 3. The grey dots are the centroid lags from all of the FR + RSS Monte Carlo (MC) based centroid lag calculations based on these same light curves. The histogram is the distribution of MC centroid lags selecting only those where peak CCF value is >0.2. A similar lag is obtained when we truncate the UV light curve to match the duration of the X-ray light curve. Such a lag time-scale is consistent with the accretion disc reverberation delay observed from other AGNs (see Sections 5 and 6 for details). Such a switch in the sign of the lag, as well as the change in lag time-scale, is remarkable.

To check the effect of UV filtering on the measured cross-correlation with X-rays, we perform the FR + RSS cross-correlation between the filtered X-ray and unfiltered UV light curve and plot the CCF lag distribution in the left-hand panel of Fig. 4 along with the X-ray/UV CCF centroid distribution with the filtered UV continuum. Clearly, X-ray and UV CCF centroid distributions using both filtered and unfiltered UV continuum significantly overlap with each other. Such an overlap implies that both fast and slow UV variability from hours to days time-scale is mostly driven by fast X-ray variability.

To explore the connection between the driving and driven variability further, we perform autocorrelation analysis using filtered X-ray, filtered and unfiltered UV light curves. The FR + RSS method and the autocorrelation distribution is shown in the right-hand panel of Fig. 4. The lag centroid distribution of all three Auto Correlation Function (ACFs) are well defined. However, the X-ray autocorrelation is significantly narrower than both filtered and unfiltered 1315 Å UV autocorrelation. Such characteristics indicate that the UV variations are smoother than that of the X-ray variability, causing a wider ACF lag distribution for UV than for X-rays.

To test whether the delays among different UV bands depend on wavelength, we carry out a further check. We consider 1315 and 1825 Å (integrated flux in 1805–1835 Å) band continuum light curves shown in the left-hand panel of Fig. 5. Both light curves have similar coverage, the same number of data points, and the variability at different time-scales is most likely driven by similar physical processes. Both light curves are mean-subtracted residuals and similar *y*-axis scales are used for an easy visual comparison of their variability. A cross-correlation between both continuum bands indicates that 1825 Å continuum lags behind the 1315 Å continuum by 0.34 ± 0.17 d, as shown in the right-hand panel of Fig. 5. We apply the filter to both light curves, decomposing them into slow and fast components separated at a 5-d time-scale. The cross-correlation between the 1315 and 1825 Å fast light curves using FR + RSS technique yields that the 1825 Å fast variability lags behind the 1315 Å fast variability by 0.04 ± 0.12 d, consistent with zero lag and shown in the left-hand panel of Fig. 6. However, when the 1315 Å slow variability is cross-correlated with the 1825 Å slow variability, the resulting distribution indicates that 1825 Å band is delayed to the 1315 Å band by 0.29 ± 0.06 d (shown in the right-hand panel of Fig. 6). Therefore, the slower variability is significantly more delayed than the faster variability in the longer UV continuum.

5 SWIFT MONITORING AND UV/OPTICAL LAG MEASUREMENTS

The log of *Swift* observations is given in Table 1. There are 176 XRT photon counting X-ray (0.5–10 keV) visits. Most of the X-ray observations were accompanied by UVOT imaging mode *UVW2* (1928 Å) observations with a lesser number including *U* (3465 Å) observations. Some UVOT observations employed the GRISM. X-ray and UV flux measurements were performed using

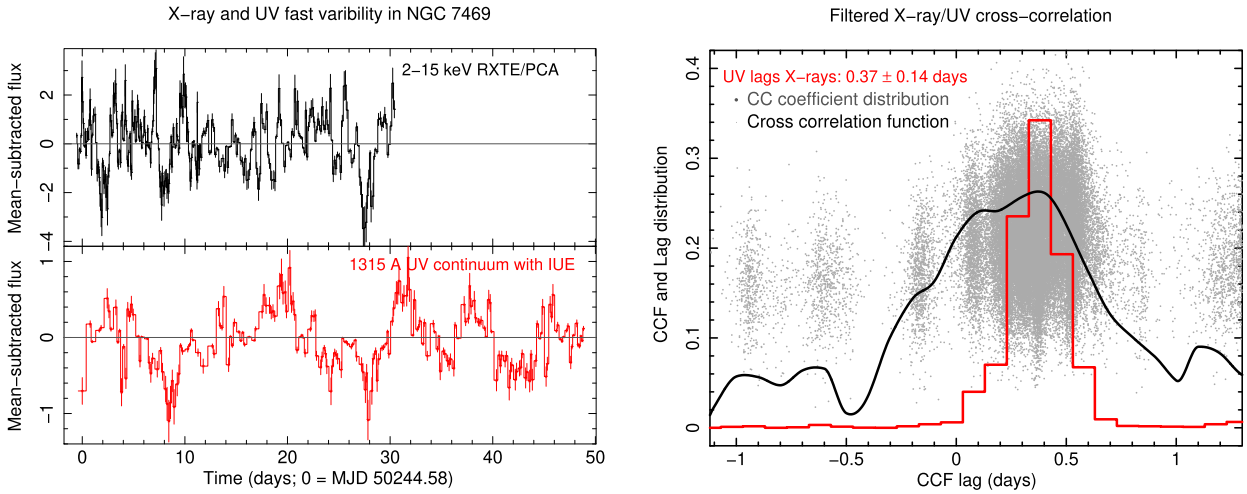

Figure 3. The effect of variability filtering: After filtering the variability longer than 5 d from X-ray and UV light curves shown in the left-hand panel of Fig. 2, the resulting light curves are shown in the left-hand panel. When these filtered light curves are cross-correlated using the MC based FR and RSS methods combined (FR + RSS), the resulting frequency distribution is shown in the right-hand panel where a switch in lag is observed at a time-scale comparable to the accretion disc reverberation time-scale. The solid line shows the interpolated CCF. The grey dots are the centroid lags from all of the FR + RSS MC based centroid lag calculations and the histogram gives the $\tau_{\rm cent}$ distribution for dots above the adopted threshold, CCF > 0.2.

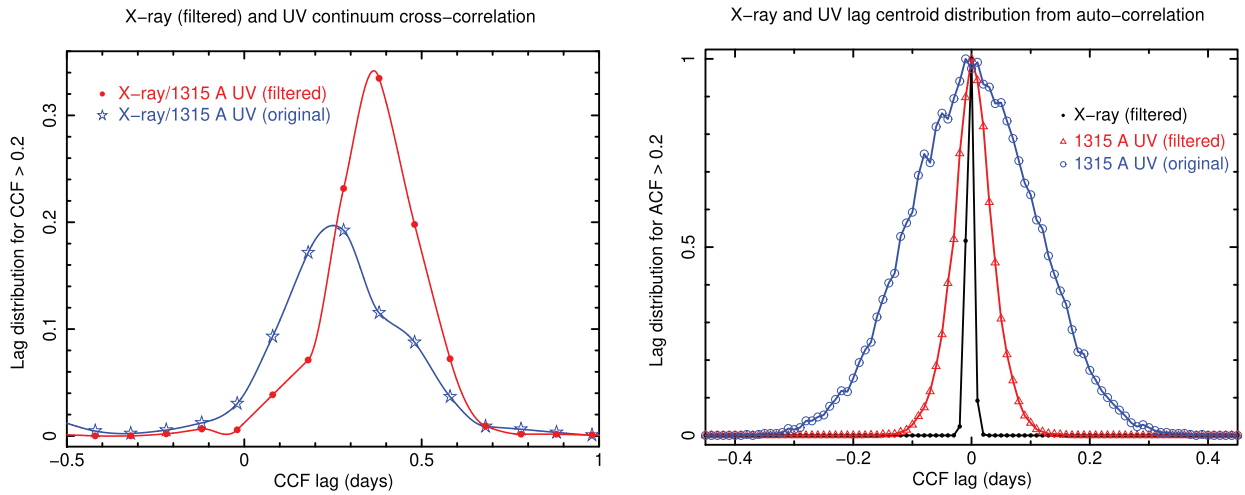

Figure 4. Effect of filtering on X-ray/UV cross-correlation: Left-hand panel shows the lag distribution for FR/RSS samples with centroid CCF >0.2 when the hi-pass filtered X-ray light curve is cross-correlated with the filtered UV continuum at 1315 Å (circles) and with the unfiltered UV continuum (stars) using the FR and RSS methods combined. A significant overlap between the two distributions can be observed. Right-hand panel shows autocorrelation distribution function of the filtered X-ray (filled circles) and both filtered (triangles) and unfiltered (empty circles) UV continuum at 1315 Å. Both filtered and unfiltered UV autocorrelation functions are wider than filtered X-ray autocorrelation function.

the Southampton pipeline[2] (McHardy et al. 2018) based on standard *Swift* data analysis procedures (Cameron et al. 2012). The X-ray, *UVW2*, and *U* filter light curves of NGC 7469 are shown in the top left panel of Fig. 7. On two occasions, *Swift* observed NGC 7469 continuously over a period of nearly 4 months in X-ray, *UVW2*, and *U* filters. One such set of observations taken between MJD 56400 and MJD 56550 is shown in the top right panel of Fig. 7. We have also extracted continuum light curves from 37 observations taken using *Swift*/GRISM between 2013 April 28 and August 20. Using GRISM data, continuum fluxes are measured at 2150, 3100, and 4600 Å, respectively, and corresponding light curves are shown in the bottom left panel of Fig. 7. For each UVOT filter and each continuum light curve from GRISM, we perform FR + RSS cross-correlation with the X-ray light curve to measure the wavelength-dependent lag. The bottom right panel of Fig. 7 shows the CCF and corresponding lag distribution computed for X-ray and *UVW2* filter (top) and for the X-ray and GRISM (bottom), respectively. We performed a wavelength-dependent cross-correlation study between the X-ray and *UVW2*, *U* filter light curves using the FR/RSS technique. With respect to the X-rays, we found that the *UVW2* and *U* filter light curves are delayed by 0.72 ± 0.51 and 1.57 ± 0.71 d, respectively. These delays are shown by empty stars in the left-hand panel of Fig. 8 while the X-ray point is shown by the solid star. Along with the *Swift* measurements, for comparison, we include the continuum UV delay from *IUE* (shown by empty circles). The lag uncertainty merely reflect the number of data points and the measurement errors in the relevant light curves.

[2]https://swiftly.soton.ac.uk/

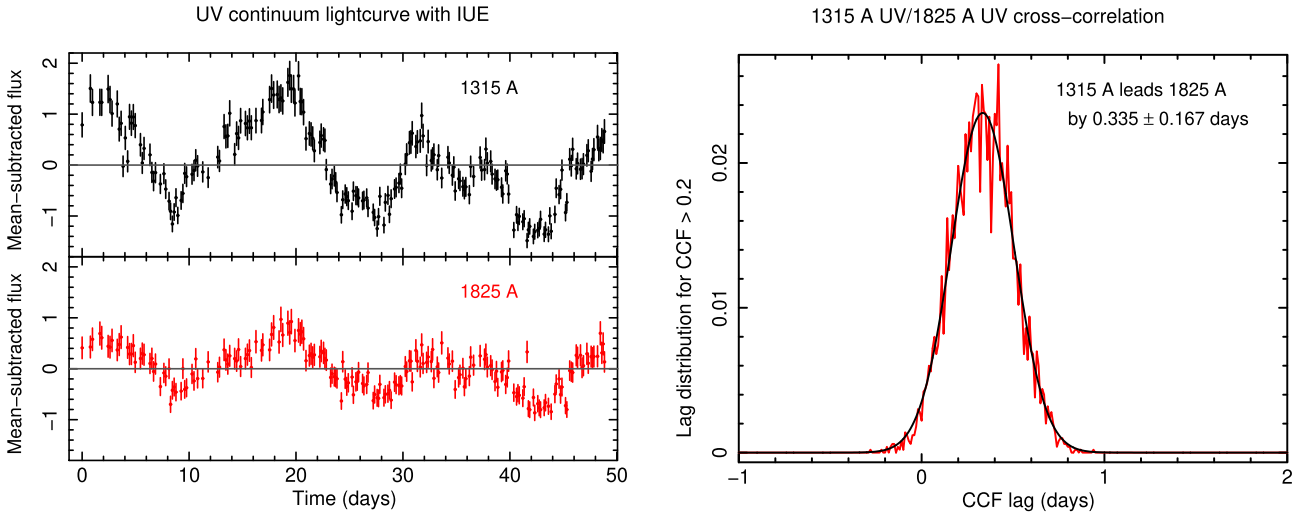

Figure 5. UV continuum light curve and CCF: Left-hand panel shows 1315 (top) and 1825 Å (bottom) UV continuum light curves from NGC 7469. Both light curves are mean-subtracted residuals and similar *y*-axis scales are used for easy comparison of their flux variability. When they are cross-correlated using FR + RSS method, the distribution of centroid lags (for CCF >0.2) is shown in the right-hand panel. The frequency distribution is fitted with a Gaussian whose centroid and the FWHM/2 are quoted as the time delay and its uncertainty, respectively.

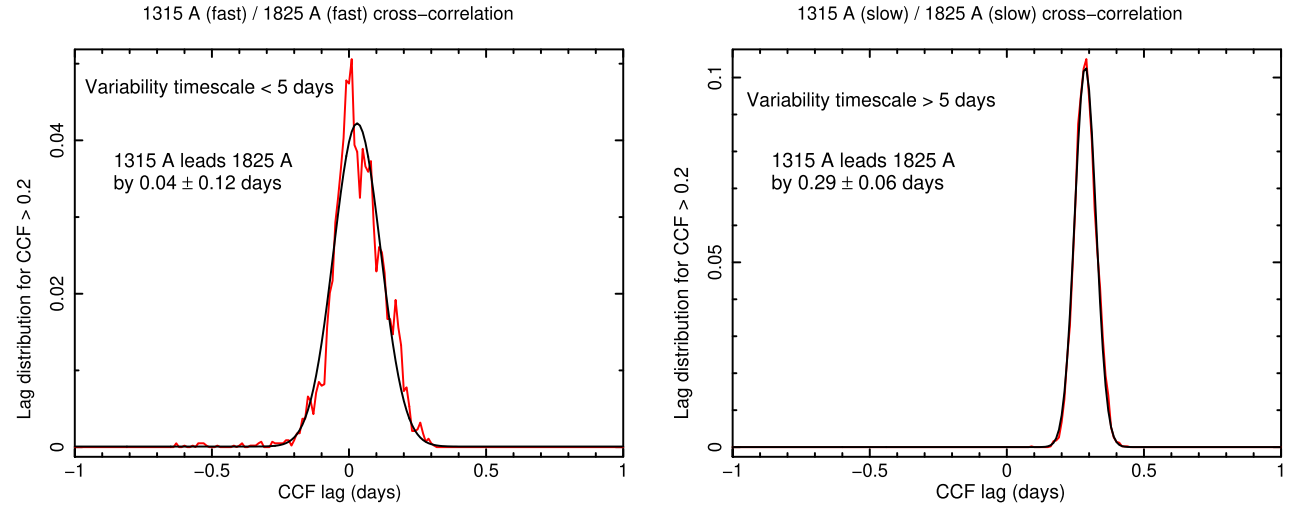

Figure 6. The effect of light-curve filtering in UV: Left-hand panel shows relative frequency distribution of CCFs computed with 1315 and 1825 Å UV continuum light curves (left-hand panel of Fig. 5) after applying a slow filter that only preserves fast (faster than 5 d) variability. On the other hand, when a fast filter is applied that only preserves slow (slower than 5 d) variability, the resulting CCF is shown in the right-hand panel. Both distributions are fitted with a Gaussian whose centroid and FWHM/2 are quoted as the time delay and its uncertainty, respectively. A significant difference between the fast and slow variability delay measurements can be noted.

We performed the FR + RSS cross-correlation between 2150 and 3100 Å and between 2150 and 4600 Å light curves, respectively, and measured the delay. To verify and confirm our results, we repeat the similar exercise of the delay measurement by replacing the 2150 Å light curve with the simultaneous *Swift*/UVW2 light curve. They are similar to within the measurement uncertainties. The resulting delays with respect to X-rays are shown by the triangles in Fig. 8. To compare fluxes during different campaigns, we compute and plot the average flux density at different wavelengths in the right-hand panel of Fig. 8. Flux densities at similar wavelengths are consistent during different campaigns.

5.1 Optical continuum from FOSC spectroscopic camera

During the *RXTE* and *IUE* joint campaign in 1996, NGC 7469 was also monitored using the Faint Object Spectroscopic Camera (FOSC) mounted on the 1 m optical telescope at the Wise Observatory, Tel Aviv University (Kaspi et al. 1996; Collier et al. 1998). Between 1996 June 2 and July 30, 42 spectroscopic observations were taken with a spectral resolution of ∼6 Å in the wavelength range 4016–7841 Å (Collier et al. 1998). While the analysis details and light curves are provided by Collier et al. (1998), the optical continuum light curves at 4845 and 6962 Å obtained from the

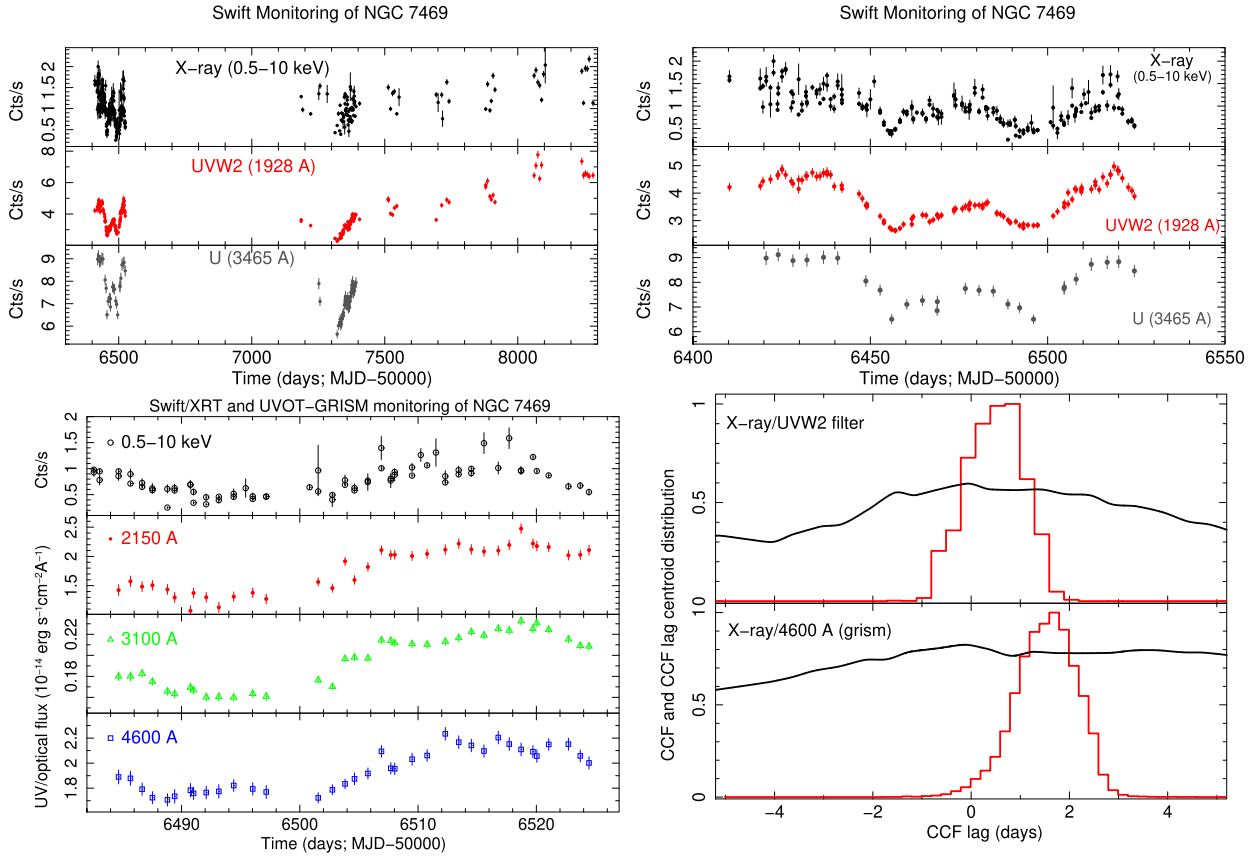

Figure 7. Reverberation delay measurements from X-ray to optical: Top left panel shows long-term (∼6 yr) light curve of NGC 7649 as monitored by *Swift*/XRT 0.5–10 keV X-ray (top) and *Swift*/UVOT *UVW2* filter at 1928 Å (middle) and *U* filter at 3465 Å (bottom). To have a visual clarity of the correlated variability among X-ray, *UVW2*, and *U* filters, a zoomed version of the same light curve between MJD 56400 and MJD 56550 is shown in the top right panel. During the same *Swift* campaign, continuum light curves obtained from *Swift*/GRISM observations at 2150, 3100, and 4600 Å are shown in the bottom left panel along with X-ray light curve. Bottom right panel shows CCF and CCF centroid distribution from FR + RSS between X-ray and *UVW2* filter light curves (top) and X-ray and 4600 Å GRISM light curve (bottom), respectively.

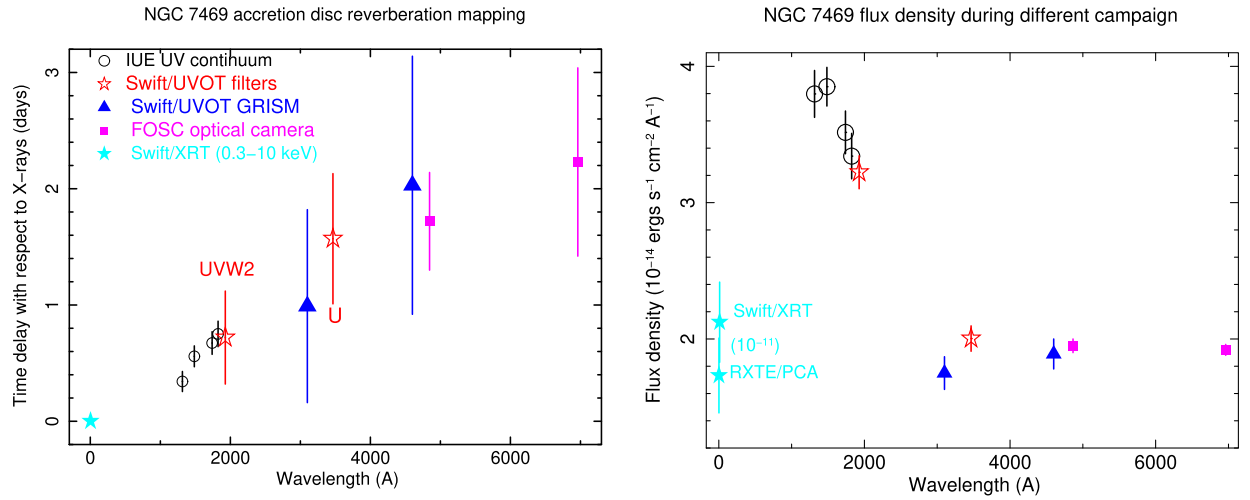

Figure 8. Reverberation delay measurements from X-ray to optical: Wavelength-dependent time delay of different UV filter and GRISM light curves with respect to the simultaneous X-ray light curve are shown by stars and triangles, respectively, in the left-hand panel. For the sake of completeness, we also include delay measurements at longer wavelength performed by the FOSC spectroscopic camera on 1 m optical telescope at the Wise Observatory partly simultaneous with the *RXTE* observations. Optical measurements are shown by squares. Empty circles are lag measurements using *IUE* continuum. Flux density measurements during different multiwavelength campaigns are shown in the right-hand panel. X-ray flux densities are shown in the unit of 10^{-11} for easy comparison. Different symbols in this panel have the same meaning as in the left-hand panel.

campaign[3] are cross-correlated with respect to the 1300 Å UV continuum light curve from *IUE* using FR + RSS technique and the resulting delays are shown by squares in Fig. 7.

6 WAVELENGTH-DEPENDENT LAG MODELLING

To understand the nature of the observed wavelength-dependent reverberation delay and test the compatibility with the prediction of standard accretion disc theory as outlined in Section 1, i.e. $\tau \propto \lambda^{4/3}$, we performed modelling using two approaches. In the first approach, shown in the top panel of Fig. 9 we fit the wavelength-dependent delay using a power-law model first optimizing both the normalization and index (shown by the dotted line) and then with the index fixed at 4/3 (shown by the solid line). While an index of 4/3 is an acceptable fit, the best-fitting index is 0.89 ± 0.09. A similar index was noted by Starkey et al. (2017) in NGC 5548. Many earlier works (Edelson et al. 2017; Cackett et al. 2018; McHardy et al. 2018) showed that the X-ray delay is usually offset with respect to the standard disc theory prediction. Therefore, in the second approach, we fit the observed delay with an offset power law (constant + powerlaw) where the offset and power-law normalization are free to vary while the index is fixed to 4/3. The resulting fit is shown in the bottom panel of Fig. 9. According to the best-fitting model the X-ray delay is offset by ∼0.38 d. Interestingly, the 1300 Å UV continuum delay is also offset by ∼0.1 d from the best-fitting prediction. Assuming the lamppost geometry of the corona, the reverberation delays at different wavelengths are calculated with respect to X-rays and shown by blue triangles with the dotted line. Details of the calculation are provided in the next section.

7 DISCUSSION AND CONCLUSIONS

In this work, we fit individual *IUE* 1220–1970 Å spectra and extract the continuum UV light curves from the model fitted parameters. Using the Monte Carlo simulation-based cross-correlation techniques, we show that the 2–10 keV X-ray light curve from *RXTE* lags behind the UV continuum light curve by 3.49 ± 0.22 d (Fig. 3). However, if we filter out variability slower than 5 d from the X-ray light curve, the cross-correlation shows that UV variability lags the X-ray variability by 0.37 ± 0.14 d. The UV lag is consistent with the same value for both filtered and unfiltered UV light curves. Such a delay time-scale is consistent with the light traveltime from the X-ray emitting corona to the UV emitting region in the accretion disc and therefore fully consistent with the accretion disc reprocessing scenario. Therefore, UV continuum variability, from hours to weeks time-scale is mainly driven by the short-term, large X-ray variability.

7.1 Evidence for finite size and temperature gradient in the reprocessing region

Between the 1315 and 1825 Å UV continuum light curves, we show (Fig. 6) that slower (>5 d) variability is delayed (0.29 ± 0.06 d) while the faster (<5 d) variability is not (0.04 ± 0.12 d). This is consistent with the accretion disc origin of UV variability at a different wavelengths. Also, the autocorrelation function is broader for UV than for X-rays (Fig. 4). Both results, delayed slow variations and broad ACF, point to UV reprocessing from an extended rather than compact region. The outer region of the reprocessed area produces slower variability while for the same wavelength emission, the inner region causes faster variability. The idea that reprocessing occurs from a hotter or larger disc was provided by McHardy et al. (2014), Fausnaugh et al. (2016), Hall et al. (2018), and Kammoun et al. (2019) and also supported by the microlensing observations (Morgan et al. 2010). If the delayed, reprocessed, UV continuum at a particular wavelength originates from a narrow region of the accretion disc, we would expect the lag distribution to be narrow and symmetric, and the UV ACF width to be similar to that of the X-rays.

7.2 Role of fast X-ray variability

Wavelength-dependent delay analysis using filtered X-ray and UV continuum light curves is found to be consistent with the predicted delay due to the reprocessed UV emission from the geometrically thin and optically thick accretion disc (Fig. 9). The inclusion of *Swift* delay measurements from NUV to optical is also consistent with the standard disc reprocessing delay, $\tau \propto \lambda^{4/3}$ relationship. Therefore, our study supports the hypothesis that the reverberation delay in the AGN accretion disc from NUV to optical is mostly driven by the X-ray variability faster than a week. The X-ray variability in AGNs is usually associated with the size of the corona, which in turns depends upon the central black hole mass and in a sample of Seyfert 1 galaxies. Lu & Yu (2001) showed that the excess variance of the short time-scale X-ray variability is anticorrelated with the black hole mass. Therefore, it suggests that in all AGNs that show reverberation continuum delays, the UV delay is driven by the fast X-ray variability, but the fast X-ray variability time-scale may vary depending upon the central black hole mass. However, testing such a hypothesis is beyond the scope of this work.

7.3 Comparison with the theoretical prediction

We have compared the measured lags (Fig. 8) with those expected following illumination of just an accretion disc by a point X-ray source located 6 R_g above the spin axis of the black hole. We use the same model as McHardy et al. (2018), i.e. we derive the temperature distribution around a black hole of a smooth accretion disc of the form described by Shakura & Sunyaev (1973). We then illuminate the disc with X-ray impulse illumination and, taking into account the resultant change in surface temperature distribution, calculate the response in various UV and optical wavebands. The X-ray impulse response is computed at six *Swift*/UVOT filter wavelengths due to the availability of their filter response curves.

As in previous work, we take the lag as the time for half of the reprocessed light to arrive (see McHardy et al. 2018 for a discussion of this point). We consider a Schwarzchild black hole and an inclination of the disc of 45 deg. We adopt a black hole mass 9×10^6 $M_\odot$ (Peterson et al. 2014) for which $L_{\rm Edd} = 1.13 \times 10^{45}$ erg s^{-1}. We take the illuminating X-ray luminosity from the *Swift*/BAT 70 month survey (Baumgartner et al. 2013) of 1.8×10^{43} erg s^{-1} and multiplied it by a factor of 2 to extrapolate from the observed 14–195 keV to a broader 0.1–500 keV band. The exact value of this parameter is not critical. The accretion rate is not well known as a central starburst ring contaminates the bolometric luminosity. Values of $\dot{m}/\dot{m}_{\rm Edd}$ between 0.05 (Mehdipour et al. 2018) and 2 (Woo & Urry 2002) have been quoted. We note that the total X-ray luminosity is then 3 per cent of the Eddington luminosity. Assuming even a very modest X-ray to bolometric correction of a factor 10 (Netzer 2019), we derive an accretion rate of $\dot{m}/\dot{m}_{\rm Edd} \sim 0.3$ and

[3] http://www.astronomy.ohio-state.edu/~agnwatch/n7469/lcv/

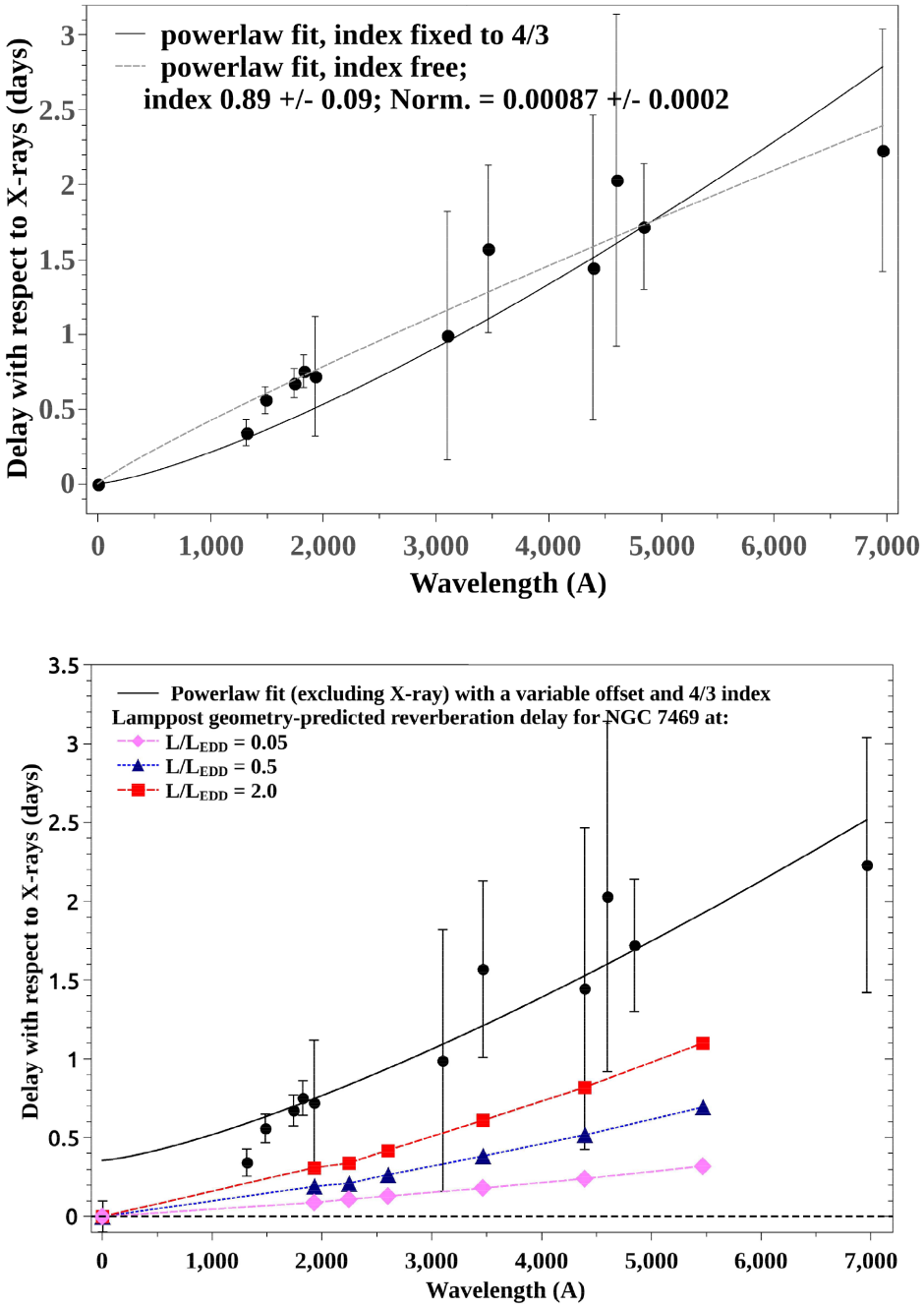

Figure 9. Reverberation delay modelling from X-ray to optical: Top panel: the fitting of wavelength-dependent delay spectrum (same spectral points as the left-hand panel of Fig. 8 but all represented by solid circles for the sake of uniformity) including X-rays using two power laws: with variable normalization and index (shown by the dotted line) and with variable normalization but fixing the index at 4/3 (shown by the solid line). Bottom panel: the power-law fit of wavelength-dependent delay with an offset where the offset and the power-law normalization are free to vary while the index is fixed to 4/3. The X-ray data point is excluded while fitting and shown for clarity. The best fit shows the X-ray and UV (1300 Å) delay measurements are below the fitted model by ∼0.38 and ∼0.1 d, respectively. Squares, triangles, and diamonds with the dotted lines show the theoretical X-ray reverberation delay estimation with $L/L_{\rm EDD}$ of 0.05, 0.5, and 2.0, respectively, for NGC 7469 assuming the 'lamppost' geometric configuration of the corona without any additional X-ray offset.

most correction factors are larger than that value. We there take $\dot{m}/\dot{m}_{\rm Edd} = 0.5$.

7.3.1 Simulation results and inference

In the top panel of Fig. 9, we plot the model theoretical values assuming $\dot{m}/\dot{m}_{\rm Edd} = 0.5$ but also show model lines covering two extremes $\dot{m}/\dot{m}_{\rm Edd}$ of 0.05 and 2. Here, we plot lags relative to the X-ray band. However, although the lags relative to the *Swift* UVW2 band generally follow a smooth curve, and are similar in most AGNs, the lag of the *UVW2* relative to the X-rays is usually much larger than expected from an extrapolation of the longer wavelength lags down to the X-ray band (McHardy et al. 2018). Here, we note similar effects. The lag spectrum dips down below a simple

power-law fit at wavelengths shorter than 2000 Å and the model lag between the *UVW*2 and *V* band (0.69 d) is a factor 2.3 less than the observed lag between *UVW*2 and *V* band derived from the simple 4/3 power-law fit to the data in Fig. 9.

Discrepancy between the observed and model lag by a similar factor just within the optical bands was first noted by Collier et al. (1999) and within the UV and optical bands by McHardy et al. (2014). As we have no observed value of the *V*-band lag, this simple model fit is our best estimate of an observed lag. A factor of 2.3 is close to the average ratio of model to observe *UVW*2 to *V*-band lags in other AGNs (McHardy et al. 2018). If we instead chose a value of $\dot{m}/\dot{m}_{\rm Edd} = 2$, the ratio between observed and model lag would drop to 1.45 and if we chose a value of $\dot{m}/\dot{m}_{\rm Edd} = 0.05$, the ratio would rise to 5. Although the lags to the longer wavelength bands are not measured here to very high precision, none the less a factor of 5 discrepancy is significantly more than seen in other AGNs whereas a factor of 1.45 would not be too different – assuming they are also all Schwarzchild black holes with disc inclinations and illuminating source heights similar to those assumed here, which are significant assumptions. We conclude that NGC 7469 does have a high accretion rate, nearer to 50 percent than 5 percent.

We may note that the above calculation assumes the delay due to the reprocessed emission in the continuum band is due to the X-ray-heated accretion disc. However, several works (Korista & Goad 2001, 2019; Lawther et al. 2018; Chelouche et al. 2019) showed that the diffuse continuum (DC) emission from the extended BLR cloud may have significant contamination in the UV-optical continuum lag measurements, particularly close to the Balmer continuum. The detail study of the DC contribution to the observed lag in NGC 7469 is beyond the scope of this work.

ACKNOWLEDGEMENTS

We thank the referee for comments and suggestions that helped to improve the clarity of the paper. MP acknowledges Royal Society-SERB Newton International Fellowship support funded jointly by the Royal Society, UK and the Science and Engineering Board of India (SERB) through Newton–Bhabha Fund. IMcH acknowledges support from a Royal Society Leverhulme Trust Research Fellowship LT160006 and from STFC grant ST/M001326/1. EMC gratefully acknowledges support from the National Science Foundation through award number AST-1909199. KH acknowledges support from STFC grant ST/R000824/1.

REFERENCES

Arev´alo P., Uttley P., 2006, MNRAS, 367, 801
Arev´alo P., Uttley P., Kaspi S., Breedt E., Lira P., McHardy I. M., 2008, MNRAS, 389, 1479
Arev´alo P., Uttley P., Lira P., Breedt E., McHardy I. M., Churazov E., 2009, MNRAS, 397, 2004
Ayres T. R., 1993, PASP, 105, 538
Baldi R. D., Behar E., Laor A., Horesh A., 2015, MNRAS, 454, 4277
Baumgartner W. H., Tueller J., Markwardt C. B., Skinner G. K., Barthelmy S., Mushotzky R. F., Evans P. A., Gehrels N., 2013, ApJS, 207, 19
Bentz M. C., Katz S., 2015, PASP, 127, 67
Bentz M. C. et al., 2009, ApJ, 705, 199
Blandford R. D., McKee C. F., 1982, ApJ, 255, 419
Breedt E. et al., 2009, MNRAS, 394, 427
Breedt E. et al., 2010, MNRAS, 403, 605
Cackett E. M., Horne K., Winkler H., 2007, MNRAS, 380, 669
Cackett E. M. et al., 2018, ApJ, 857, 53
Cameron D. T., McHardy I. M., Dwelly T., Breedt E., Uttley P., Lira P., Arevalo P., 2012, MNRAS, 422, 902
Chelouche D., Pozo N., Francisco K. S., 2019, Nat. Astron., 3, 251
Cleveland W. S., Devlin S. J., 1988, J. Am. Stat. Assoc., 83, 596
Collier S. J. et al., 1998, ApJ, 500, 162
Collier S. J., Horne K., Wanders I., Peterson B. M., 1999, MNRAS, 302, L24
Dai X., Kochanek C. S., Chartas G., Kozlowski S., Morgan C. W., Garmire G., Agol E., 2010, ApJ, 709, 278
Dexter J., Agol E., 2011, ApJ, 727, L24
Edelson R. et al., 2015, ApJ, 806, 129
Edelson R. et al., 2017, ApJ, 840, 41
Edelson R. et al., 2019, ApJ, 870, 123
Epanechnikov V. A., 1969, Theory Probab. Appl., 14, 153
Fausnaugh M. M. et al., 2016, ApJ, 821, 56
Gardener E., Done C., 2017, MNRAS, 470, 3591
Hall P. B., Sarrouh G. T., Horne K., 2018, ApJ, 854, 93
Kammoun E. S. et al., 2019, ApJ, 879, 24
Kaspi S., Ibbetson P. A., Mashal E., Brosch N., 1996, Wise Obs. Tech. Rep., 6
Korista K. T., Goad M. R., 2001, ApJ, 553, 695
Korista K. T., Goad M. R., 2019, MNRAS, 489, 5824
Kotov O., Churazov E., Gilfanov M., 2001, MNRAS, 327, 799
Kriss G. A., Blustin A., Branduardi-Raymont G., Green R. F., Hutchings J., Kaiser M. E., 2003, A&A, 403, 473
Lawther D., Goad M. R., Korista K. T., Ulrich O., Vestergaard M., 2018, MNRAS, 481, 533
Lu Y., Yu Q., 2001, MNRAS, 324, 653
Marshall K., Ryle W. T., Miller H. R., 2008, ApJ, 677, 880
McHardy I. M., Uttley P., Mason K., Page M., 2003, in Collin S., Combes F., Shlosman I., eds, ASP Conf. Ser. Vol. 290, Active Galactic Nuclei: from Central Engine to Host Galaxy. Astron. Soc. Pac., San Francisco, p. 111
McHardy I. M., Papadakis I. E., Uttley P., Page M. J., Mason K. O., 2004, MNRAS, 348, 783
McHardy I. M. et al., 2014, MNRAS, 444, 1469
McHardy I. M. et al., 2018, MNRAS, 480, 2881
Mehdipour M. et al., 2018, A&A, 615, A72
Morgan C. W., Kochanek C. S., Morgan N. D., Falco E. E., 2010, ApJ, 712, 1129
Mosquera A. M., Kochanek C. S., Chen B., Dai X., Blackburne J. A., Chartas G., 2013, ApJ, 769, 53
Nandra K., Clavel J., Edelson R. A., George I. M., Malkan M. A., Mushotzky R. F., Peterson B. M., Turner T. J., 1998, ApJ, 505, 594
Narayan R., 1996, ApJ, 462, 136
Netzer H., 2019, MNRAS, 488, 5185
Nichols J. S., Garhart M. P., de la Pena M. D., Levay K. L., 1993, NEWSIPS Information Manual : Low-Dispersion Data v1.0, CSC/SD-93/6062
Noda H. et al., 2016, ApJ, 828, 78
Pal M., Naik S., 2018, MNRAS, 414, 5351
Pal M., Dewangan G. C., Connolly S., Misra R., 2017, MNRAS, 466, 1777
Papadakis I. E., Nandra K., Kazanas D., 2001, ApJ, 554, 133
Peterson B. M., 2014, Space Sci. Rev., 183, 253
Peterson B. M., Wanders I., Horne K., Collier S., Alexander T., Kaspi S., 1998, PASP, 110, 660
Peterson B. M. et al., 2004, ApJ, 613, 682
Peterson B. M. et al., 2014, ApJ, 795, 149
Petrucci P. O., Maraschi L., Haardt F., Nandra K., 2004, A&A, 413, 477
Poole T. S. et al., 2008, MNRAS, 383, 627
Salamanca I., Alloin D., Pelat D., 1995, A&AS, 111, 283
Shakura N. I., Sunyaev R. A., 1973, A&A, 24, 337
Shappee B. J. et al., 2014, ApJ, 788, 48
Shemmer O., Uttley P., Netzer H., McHardy I. M., 2003, MNRAS, 343, 1341
Shull J., Michael S., Matthew D., Charles W., 2012, ApJ, 752, 162
Starkey D. et al., 2017, ApJ, 835, 65
Sun M., Xue Y., Cai Z., Guo H., 2018, ApJ, 857, 86

Troyer J., Starkey D., Cackett E. M., Bentz M. C., Goad M. R., Horne K., Seals J. E., 2016, MNRAS, 456, 4040
Uttley P., Edelson R., McHardy I. M., Peterson B. M., Markowitz A., 2003, ApJ, 584, L53
Uttley P., Wilkinson T., Cassatella P., Wilms J., Pottschmidt K., Hanke M., Bock M., 2011, MNRAS, 414, L60
Vestergaard M., Wilkes B. J., 2001, ApJS, 134, 1
Wanders I. et al., 1997, ApJS, 113, 69
Welsh W. F., 1999, PASP, 111, 1347
White R. J., Peterson B. M., 1994, PASP, 106, 879
Woo J.-H., Urry C. M., 2002, ApJ, 579, 530
Zu Y., Kochanek C. S., Peterson Bradley M., 2011, ApJ, 735, 80

This paper has been typeset from a TEX/LATEX file prepared by the author.